1-1-2019

Microstructure evolution and electrochemical properties of TiO 2 /Ti-35Nb-2Ta-3Zr micro/nano-composites fabricated by friction stir processing

Hao Gu

Zihao Ding

Zhi Yang

Weiqiang Yu

Wenjie Zhang

See next page for additional authors

10.1016/j.matdes.2019.107680

Gu, H., Ding, Z., Yang, Z., Yu, W., Zhang, W., Lu, W., . . . Fu, Y. -. (2019). Microstructure evolution and electrochemical properties of TiO 2 /Ti-35Nb-2Ta-3Zr micro/nano-composites fabricated by friction stir processing. Materials and Design, 169. Available here

Materials and Design 169 (2019) 107680

Contents lists available at ScienceDirect

Materials and Design

journal homepage: www.elsevier.com/locate/matdes

Microstructure evolution and electrochemical properties of TiO_2/Ti-35Nb-2Ta-3Zr micro/nano-composites fabricated by friction stir processing

Hao Gu [a,1], Zihao Ding [b,c,1], Zhi Yang [a,1], Weiqiang Yu [a], Wenjie Zhang [a], Weijie Lu [b], Lai-Chang Zhang [d,*], Kuaishe Wang [e,*], Liqiang Wang [b,*], Yuan-fei Fu [a,*]

[a] Department of Prosthodontics, Shanghai Ninth People's Hospital, College of Stomatology, Shanghai Jiao Tong University School of Medicine; National Clinical Research Center for Oral Diseases; Shanghai Key Laboratory of Stomatology and Shanghai Research Institute of Stomatology, Shanghai 200011, China
[b] State Key Laboratory of Metal Matrix Composites, Shanghai Jiao Tong University, Shanghai 200240, China
[c] Department of Materials Science and Engineering, Carnegie Mellon University, 5000 Forbes Avenue, Pittsburgh, PA 15213, USA
[d] School of Engineering, Edith Cowan University, 270 Joondalup Drive, Joondalup, Perth, WA 6027, Australia
[e] School of Metallurgical Engineering, Xi'an University of Architecture and Technology, Xi'an 710055, China

HIGHLIGHTS

- Composite layers possess nanocrystallines and amorphous phases with homogeneous dispersive oxygen.
- Composite layers show α″ martensites and dislocations with dynamic recrystallization.
- More titanium oxides of high valence were discovered in surface of oxide films of composite layers.
- Dense needlelike structure was observed on surface of composite layers after polarization.
- Corrosion resistance is optimized by modified microstructure with increase of rotation speed and TiO_2 added.

GRAPHICAL ABSTRACT

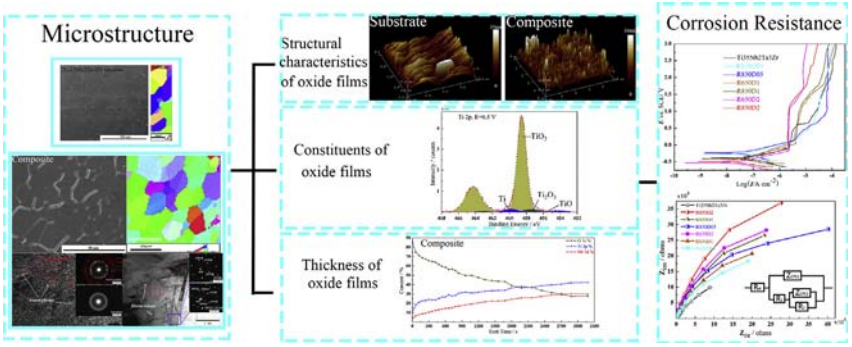

ARTICLE INFO

Article history:
Received 23 October 2018
Received in revised form 31 January 2019
Accepted 26 February 2019
Available online 26 February 2019

Keywords:
Friction stir processing
Titanium alloys
Micro/nano-composites
Surface modification
Corrosion resistance

ABSTRACT

Forming stable anti-corrosion surface layer and homogenized microstructure on the surface of material has become a major challenge in developing biomedical β titanium alloy. In the study, TiO_2/Ti-35Nb-2Ta-3Zr anti-corrosion micro/nano-composites with different amount of TiO_2 particles were successfully fabricated by one-pass friction stir processing (FSP). The composition, microstructure and electrochemical properties of the material are characterized systematically. In particular, compact passive oxide films formed on surface of the material after electrochemical corrosion are elaborated from constituent, thickness and structural characteristics. Furthermore, the relationship between various FSP parameters, microstructure presented and corresponding corrosion resistance has been discussed in detail. The results show that TiO_2/Ti-35Nb-2Ta-3Zr micro/nano-composite layers possess massive uniform β grains with homogeneous dispersive oxygen on the surface. Nanocrystallines surrounded by amorphous phases and α″ martensite accompanied with dislocations are discovered. TiO_2/Ti-35Nb-2Ta-3Zr micro/nano-composite layers present outstanding corrosion resistance. More TiO_2 added and

* Corresponding authors.
E-mail addresses: lczhangimr@gmail.com (L.-C. Zhang), wangkuaishe888@126.com (K. Wang), wang_liqiang@sjtu.edu.cn (L. Wang), fuyuanf@163.com (Y. Fu).
[1] These authors contributed equally to this work.

https://doi.org/10.1016/j.matdes.2019.107680

higher rotation speed promotes the optimization in corrosion resistance forming more compact passive films. The study displays the potential of a new micro/nano-composite with outstanding surface microstructure and corrosion resistance that serves better as a biomedical implant.

1. Introduction

β titanium and its bio-derived materials reveal great potential as implants owning to their high strength, low Young's modulus, outstanding corrosion resistance and splendid biocompatibility [1–3]. As a quaternary system, Ti-Nb-Ta-Zr β titanium alloys (TNTZ) exhibit improvement in mechanical and corrosion properties compared with pure Ti. With the addition of Nb, Ta and Zr elements, thermal stability of the material is enhanced, and meanwhile chemical dissolution of the oxide film is also reduced [4–8]. In particular, the tensile strength of Ti-35Nb-2Ta-3Zr after cold-rolling can reach 896.26 MPa, while its elastic modulus drops down below 50 GPa [9].

The formation of a stable and compact oxidation film on the surface of titanium alloys, which essentially consists of TiO_2, can well retard the corrosion [10]. However, TiO_2 layer naturally formed on the surface of implants in service is thin and irregular, thus is vulnerable to inevitable abrasion with body hard tissues [11]. Moreover, the oxidation film is likely to peel off under cyclic stress due to weak bonding with the substrate [12]. The dissolution of oxide film occurs indeed in Cl^- concentrate solution, as a result of the competitive adsorption between Cl and O ions [13–15]. Thus, to a great extent, structures and bonding of surface TiO_2 layer determine the corrosion resistance of titanium alloys.

Recently, different surface modification methods have been used to optimize surface properties, such as ion implantation, spark plasma sintering, powder sintering [16–20]. Friction stir processing (FSP), which is a relatively new localized thermomechanical processing technique, can fabricate micro/nano-sized structure in surface of substrate with advantage [21]. The refinement and homogenization of grains are available during the process, owing to the local intense plastic deformation and stirring heat caused by FSP [22,23]. The improvement on microstructure and mechanical properties eliminates defects of the substrate. Moreover, micro/nano-composite surface layer processed by FSP obtains much stronger bonding with base metal compared with other modification methods [24]. In the process of corrosion, refined surface microstructure could increase the compactness of surface oxide films so as to inhibit corrosion.

It is reported that when incorporated into micro/nano-composites as reinforcement, TiO_2 can help change the surface morphology, improve mechanical properties and enhance corrosion resistance of the material [25,26]. Some recent researches have showed that the hybrid composites on the aluminum alloy AA7075 displayed better strength and dimensional stability with the increase in TiO_2 concentration through grain refinement [27]. In addition, TiO_2 coating could promote biocompatibility and corrosion resistance compared with pure Ti in SBF solution [28]. Besides, as we know, TiO_2 as an important role in superficial oxide films may be beneficial to impede corrosion. Therefore, TiO_2 micro-nanoscale reinforcement is expected to enhance both mechanical properties and corrosion resistance of the material, on account of its special chemical inertia and strong bonding realized by FSP.

The previous researches have demonstrated good corrosion resistance, cell adhesion and proliferation of Ti-35Nb-2Ta-3Zr [29]. Subsequently, Wang et al. [30] enhanced microhardness of the titanium alloy and attributed it to interaction mechanism of dislocations, twinning, deformation induced α″ and ω phases. With respect to TiO_2 micro/nano-composite layers by FSP, our team explored the microstructure, microhardness, corrosion resistance and biocompability of micro/nano-composites of Ti-6Al-4 V and TiO_2 fabricated by FSP rotated at the speed of 375 r/min [31,32]. Similarly, Yang et al. [33] proved that Ag micro/nano-composite layers modified by FSP optimized antibacterial property and cell adhesion, at the same time microstructure evolution, and electrochemical property of the material were detailed discussed. These researches about Ti-35Nb-2Ta-3Zr substrate and metal matrix composites presented a desired potential of further optimization of mechanical properties and corrosion resistance of Ti-35Nb-2Ta-3Zr substrate.

While numerous researches proved that it's feasible to realize surface modification and improve material properties of biomaterial titanium alloys through FSP, due to the complexity of this process, the influences of technology parameters during FSP, such as rotation speed and the amount of reinforcement particles, have been rarely discussed. Besides, most researches just attributed promotion of corrosion resistance to surface refinement but were lack of overall systematic analyses.

In this study, FSP was utilized to incorporate TiO_2 particles into Ti-35Nb-2Ta-3Zr biomedical titanium alloy to form a metal matrix micro/nano-composite surface layer. This work systematically explored the effect of FSP parameters on microstructure and corrosion property of TiO_2 micro/nano-composite layer, and meanwhile the correlation between them and corrosion resistance mechanism were detailed discussed. Besides, to investigate the possible scenarios caused by different FSP technology parameters, various depths of incorporated particles (0.5, 1 and 2 mm) and rotation speeds (650 rpm and 850 rpm) were taken into account. This study provided a new insight into the surface modification of composite layer through FSP for potential of medical use as a novel implant biomaterial.

2. Experimental procedures

2.1. Material preparation and friction stir processing

Ti-35Nb-2Ta-3Zr alloys with 99.5 wt% purity were fabricated under argon shielding. The ingot was melted thrice at 1223 K for 1 h in vacuum condition and casted into a billet, which was solution treated at 780 °C for 30 min. The metal plate with a thickness of 5 mm was obtained after air cooling and rolling at room temperature with the 90% total rolling reduction ratio to eliminate stress produced in the machining process and get a stable β phase matrix. The ordered holes in the forward direction were grooved by wire cutting in a line at an interval of 3 mm on surface of the metal plate after polishing and cleaning.

TiO_2 powder (99% purity with an average diameter of 200 nm) was filled in the holes. In order to explore the effect of various contents of TiO_2 particles, same size holes with a diameter of 1 mm were punched with different depths (0.5 mm, 1 mm and 2 mm) and then the holes were filled with TiO_2 powder. To fabricate the metal matrix composites, FSP was applied by a professional FSW machine, which consisted of a tungsten steel shoulder and a pin. The diameter of the shoulder was 15 mm. The diameter and plunge depth of the pin were 10 mm and 2 mm respectively, which was tilted by 2.5° during FSP [30]. As shown in Fig. 1, the probe moved at a constant travel speed of 50 mm/min and two rotation speeds, 650 rpm and 850 rpm were selected. The whole process was conducted in the argon protecting atmosphere to avoid oxidation. The experimental samples were named as R650D05, R650D1, R650D2, R850D05, R850D1 and R850D2 according to various rotation speeds and depths during FSP. For example, the R650D05 represented the rotation speed of 650 rpm and depth of 0.5 mm.

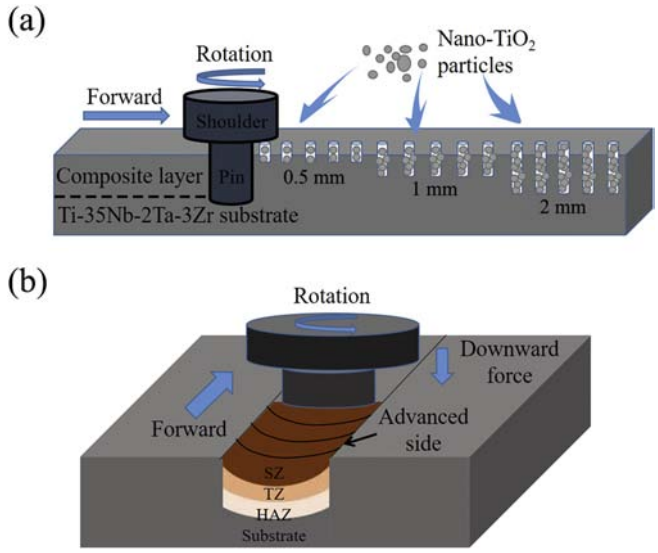

Fig. 1. Fabrication of TiO_2/Ti-35Nb-2Ta-3Zr metal matrix micro/nano-composite: (a) Different addition depths of TiO_2 particles, and (b) Schematic of friction stir processing.

2.2. Microstructural characterization

The materials after FSP were cut into 7 mm × 7 mm samples by wire electrical discharge machining, and prepared in an epoxy mount. After polishing, the samples were etched in a solution composed of 10 vol% HF, 30 vol% HNO_3, and 60 vol% H_2O. Microstructure observations were carried out by a Nova FEI 400 field emission scanning electron microscope (SEM) in secondary electron and backscattering modes and high resolution TEM (HRTEM) with a JEM2100 microscope operating at 200 kV. To carry out Electron backscattered diffraction (EBSD), the samples were further ion polished for 8 h after mechanical polishing and vibration polishing in order to eliminate surface stress. EBSD analysis was executed at 20 kV and 8 nA with a 70° angle of inclination in a Nova FEI 400 field emission SEM with HKL Channel Oxford 5 EBSD system, with a scan step size of 1 μm and a spot size of 5 nm. The setting of the grain tolerance angle used for grain-size measurements was 5° and the lower limit of boundary-misorientation cutoff was 2° for misorientation measurements [30].

2.3. X-ray diffraction and energy dispersive spectroscopy

The samples for XRD and EDS analyses were cleaned beforehand by ethanol and deionized water in an ultrasonic bath for 3 min. The phase analysis was carried out by X-ray diffraction (XRD) in a D8 ADVANCE Da Vinci XRD device at 40 kV and 40 mA. The scanning range (2θ) was from 10° to 90° and the scanning rate was 0.08°/min, with a step of 0.02° using $CuK_\alpha\lambda = 1.5406$ Å radiation. Energy dispersive spectroscopy (EDS) was conducted in a Nova FEI 400 field emission SEM equipped with an energy dispersive spectrometer for elemental mapping.

2.4. Electrochemical measurements

The potentiodynamic polarization (POT) and electrochemical impedance spectroscopy (EIS) tests were measured with the electrochemical workstation PARSTAT 2273. The whole process was performed in a three-electrode cell with a saturated calomel electrode (SCE) as the reference electrode, a platinum electrode as the auxiliary electrode and an experimental sample as the working electrode. The area of the samples exposed in the solution is 0.49 cm^2. Hank's solution was chosen to simulate body fluid environment [34]. The solution was composed of 8 g/l NaCl, 0.4 g/l KCl, 0.14 g/l $CaCl_2$, 0.35 g/l $NaHCO_3$, 0.06 g/l $Na_2HPO_4 \cdot 2H_2O$, 0.1 g/l $MgCl_2 \cdot 6H_2O$, 0.06 g/l KH_2PO_4, 0.06 g/l $MgSO_4 \cdot 7H_2O$ and 1 g/l glucose. The pH of solution was regulated to approximately 7.4. During the measurement, the temperature was kept at 37 °C. In order to get a relatively stable state, the open circuit potential (OCP) measurements maintained 1.5 h. The EIS was measured with the 10 mV signal amplitude from high frequency of 100 kHz to low frequency of 10 mHz. The potentiodynamic polarization tests were measured at a step height of 1 mV and a scan rate of 1 mV/s from an initial potential of −0.25 V vs. OCP to the final potential of 3 V. The recorded data were analyzed by Power Suite software and the EIS data were curve fitted by ZSimpWin 3.21 software.

2.5. AFM (Atomic Force Microscope) measurements

AFM measurements were carried out by Dimension Icon & FastScan Bio AFM device. The samples after potentiodynamic polarization were cleaned three times by deionized water gently so as to wipe off superficial deposits before observation. Tapping mode was used for topography measurements. Local dc current was mapped via an infliction of 25 mV bias voltage between the probe and the conductive base. The NanoScope Analysis 1.8 software was used for analysis of the data and maps.

2.6. XPS measurements of surface and depth profile

X-ray photoelectron spectroscopy (XPS) measurements were carried out by an AXIS UltraDLD XPS apparatus with a monochromatic Al Kα X-ray source. The resolution of spectrometer was 0.48 eV, as measured on an Ag $3d_{5/2}$ peak. The values of binding energy were calibrated by the C 1 s peak value (284.6 eV). The depth profile analyses of oxide layers were performed after the surface detections. The sputtering was conducted by the Ar^+ ion beam at a rate of 2 nm/min determined on the SiO_2 standard. The samples were corroded at the constant potential of 0.5 V for 1.5 h after the measurements of OCP for 1.5 h. The data were analyzed by CasaXPS software.

3. Results

3.1. Microstructure characteristics

Fig. 2 shows SEM micrographs and element compositions of the surface of Ti-35Nb-2Ta-3Zr alloy and FSPed samples (R650D05 and R850D05). Coarse grains with an average grain size of approximately 80 μm are observed on the surface of Ti-35Nb-2Ta-3Zr substrate in Fig. 2a. Compared with the substrate, massive uniform and finer equiaxed β grains with a mean size of 8 μm on the surface of stir zone were acquired by FSP, which indicates the occurrence of grain refinement, as shown in Fig. 2b and Fig. 2c. There is no obvious difference of morphology between R650D05 and R850D05 samples. In addition, Fig. 2d, e and f show EDS analyses and detailed data are recorded in Table 1. The element mappings of the surface of stir zone in R650D05 and R850D05 display directly the uniform distribution of oxygen in the insets of Fig. 2e and f. As shown in Fig. 3a and b, few second phases can be observed in surface of stir zones in R650D05 and R850D05 samples in BSE mode marked by red circles, while, the structure of other tissues is homogeneous. Due to higher rotation speed, as shown in Fig. 3b, the clusters in R850D05 samples are more uniform and tiny (about 0.3 μm), compared with those in R650D05 samples (about 0.5 μm). This indicates that high rotation speed inhibited partial accumulation of TiO_2 particles. Similar results were discovered by Rajeshkumar et al. [35]. They attributed the highly dispersed distribution to more dislocation and deformation generated at a higher rotation speed during FSP, which facilitated refinement of grains and homogeneous microstructure. Fig. 3c is line scanning of the second phase. Compared with surrounding tissues, the oxygen content of the second phase zone has increased and the titanium content has correspondingly decreased at the same time. However, due to the interaction volume of beam, the element content can be influenced by precipitates nearby or under the surface [36]. Besides, the spatial resolution of SEM-EDS is limited to about 2 μm so that the tiny clusters could not be detected precisely.

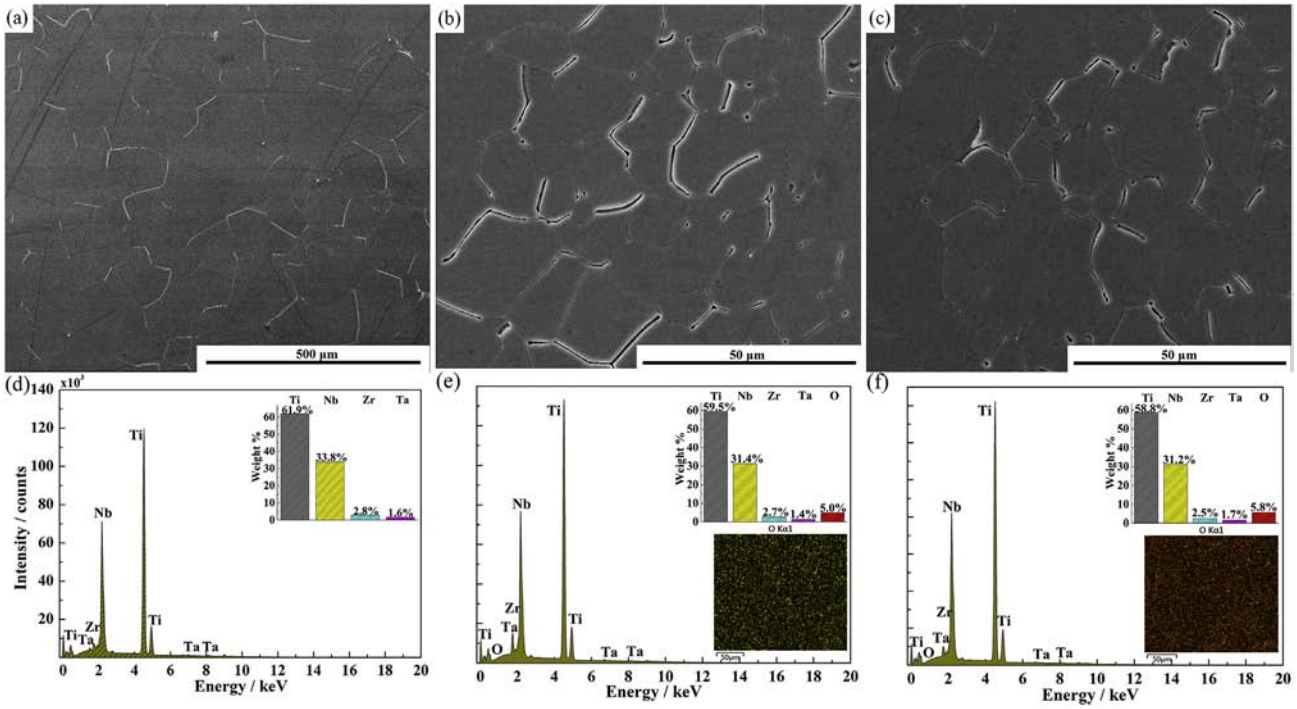

Fig. 2. SEM images of morphology features and corresponding element distribution: (a) surface of Ti-35Nb-2Ta-3Zr substrate, (b) surface of TiO_2 micro/nano-composite layers of R650D05, (c) surface of TiO_2 micro/nano-composite layers of R850D05, (d) element spectra for Ti-35Nb-2Ta-3Zr substrate, (e) element spectra for R650D05 and (f) element spectra for R850D05, with insets of oxygen element mappings.

Table 1
Element compositions (wt%) of Ti-35Nb-2Ta-3Zr substrate and FSP groups by EDS analyses.

Groups	Ti (wt%)	Nb (wt%)	Ta (wt%)	Zr (wt%)	O (wt%)
Substrate	61.9	33.8	1.6	2.8	–
R650D05	59.5	31.4	1.4	2.7	5.0
R650D1	58.2	31.7	1.7	2.7	5.7
R650D2	57.8	31.5	1.6	2.6	6.5
R850D05	58.8	31.2	1.7	2.5	5.8
R850D1	58.2	31.3	1.8	2.6	6.1
R850D2	58.3	30.5	1.5	2.7	7.0

Therefore, it is only speculated that the composition of the clusters could be related to oxygen in view of the consistency of fluctuations.

In order to explore deeply the effect on microstructure of TiO_2 composite layers by FSP, TEM micrographs of modified surface of FSPed samples were obtained. In Fig. 4, massive dislocation and deformation are discovered both in R650D05 and R850D05 samples. Fig. 4a and b show no distinct anisotropy and uniform grains on surface of stir zones in R650D05 and R850D05 samples. A mass of dislocations extend from grain boundaries to grain internal and interlace to form dislocation tangles in Fig. 4c and d. As shown in Fig. 4e and f, many slip bands are observed in the grain. Dislocations mostly slide in slip bands and planes, and multiple overlapping dislocations can lead to the formation of wavy and wide slip bands. A number of short and meandering slip traces caused by dislocations are shown in Fig. 4e (marked by arrows). Many dense and paralleled slip bands are in grains on surface of R850D05 in Fig. 4f. This could attribute to more severe plastic deformation induced by higher rotation speed. Meanwhile, due to lower basal plane stacking faults energy, adding TiO_2 particles can decrease the basal plane stacking faults energy of the whole system so as to more formation of dislocation [37]. For R850D05 samples, more microstructure details are presented in Fig. 5. Recrystallized grains on the modified surface of stir zone in R850D2 are shown by red line in Fig. 5a, which are attributed to consecutive extrusion and dislocations of surrounding grains. Meanwhile,

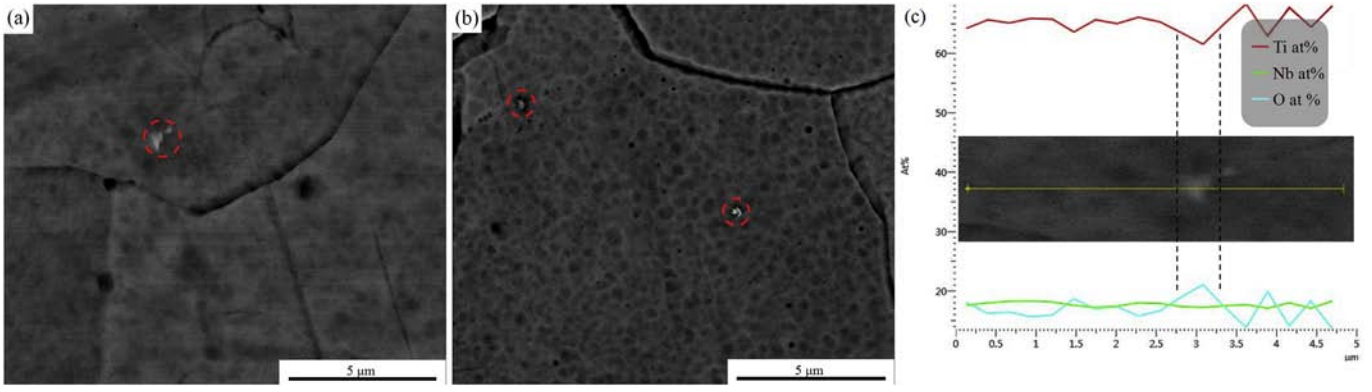

Fig. 3. SEM images and element analysis of reinforcement: (a) reinforcement on surface of R650D05, (b) reinforcement on surface of R850D05, (c) element analysis by linear scan of reinforcement in Fig. 3a.

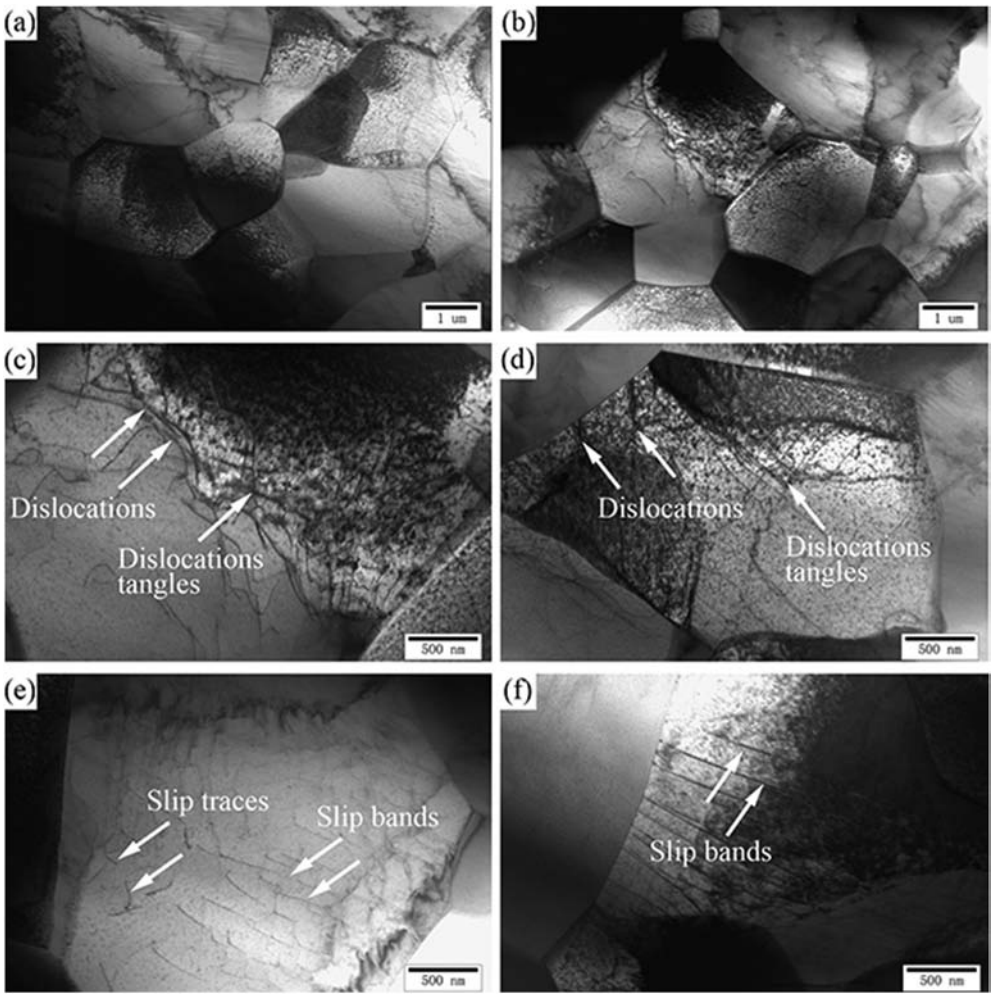

Fig. 4. TEM images of microstructure in surface of TiO_2 micro/nano-composite layers: (a) refined grains in R650D2, (b) refined grains in R850D2, (c) dislocation and dislocation tangles in R650D2, (d) dislocation and dislocation tangles in R850D2, (e) bright images of slip bands and traces in R650D2, (f) bright images of slip bands and traces in R850D2.

dislocation tangles appear around the recrystallized grain boundaries as marked by arrows in Fig. 5b. In Fig. 5c and d, HRTEM images of recrystallized grains in surface of stir zones are presented accompanied with the SAED (selected area electron diffraction) patterns. As is seen in Fig. 5c, β phases with an interatomic distance of 0.253 nm are presented. Fig. 5d shows the magnified image of the region marked by the square in Fig. 5c. Several nanocrystallines with regular atomic arrangement surrounded by amorphous phases could be observed. The relative SAED patterns also indicate the existence of nanocrystallines and amorphous phases. Meanwhile, the diffraction rings reveal that the nanocrystalline structure is β-Ti. Similar micromorphology of nanocrystalline and amorphous phase was found by Zhang and Ran [31,38]. Zhang considered that the TiO_2 composites transformed into amorphous structure under the continual plastic deformation introduced by FSP. Ran attributed the formation of amorphous phases to the dissolution of oxygen and intense plastic flow during FSP. Same as the second phases in Fig. 3a and b, a tiny particle of about 90 nm in diameter can be seen in Fig. 5e. According to element analyses of the particle in Fig. 5f, the atomic ratio of oxygen and titanium is close to 2 to 1, so it can be considered that the second phases in the SEM and TEM figures are TiO_2 particles.

Fig. 6a shows the XRD spectrum of surface of Ti-35Nb-2Ta-3Zr substrate, R650D1 and R850D1 samples. In addition to β phases, martensites in FSPed samples were detected by XRD. As shown in Fig. 6b, typical needle-shaped α″ martensites are discovered in surface of stir zones. The corresponding SAED patterns show the orientation relationship between β-Ti and α″ martensite. Besides, many dislocations are revealed around α″ martensites. The reason for the formation of martensites could be attributed to internal stress field caused by the non-uniform deformation of grains and appearance of tangled dislocations, which promoted the nucleation and transformation of martensites [39]. Compared with R650D1 sample, the intensity of α″ martensite peak (020) has increased apparently in R850D1 sample, showing positive relationship between α″ martensite transformation and rotation speed. That is because more plastic deformation and internal stress field induced by high rotation speed could promote nucleation of martensites [40].

More microstructure characteristics of grains on the surface of Ti-35Nb-2Ta-3Zr substrate and surface of stir zone in FSPed samples (R650D05 and R850D05 samples) are revealed by EBSD analysis in Fig. 7. Different from petaliform coarse grains in the substrate, uniform equiaxed β grains with some scattered fine recrystallized grains in the TiO_2 micro/nano-composite layer are presented in Fig. 7a. As shown in Fig. 7c, the similar grain sizes of FSPed samples (8.54 μm for R650D05 and 8.87 μm for R850D05 respectively) are found, which are 10 times smaller than the size of substrate. The mean grain size of modified surface of R850D05 is slightly larger than that of R650D05. This could be for the reason that under same cooling condition, a higher surface temperature generated by higher rotation speed and more extreme friction leaded to a faster temperature drop at the very beginning, so that grains absorbed more friction heat [41]. Although not intuitively visible, through the grain-size measurements of EBSD, there are indeed few grains of hundreds nanometers in surface of micro/nano-composite layers, accounting for about 15%. The distribution of misorientation angle is shown in Fig. 7d. The average misorientation angle is 22.34° and the fraction of high angle grain boundaries (HAGBs) is 62.12% in

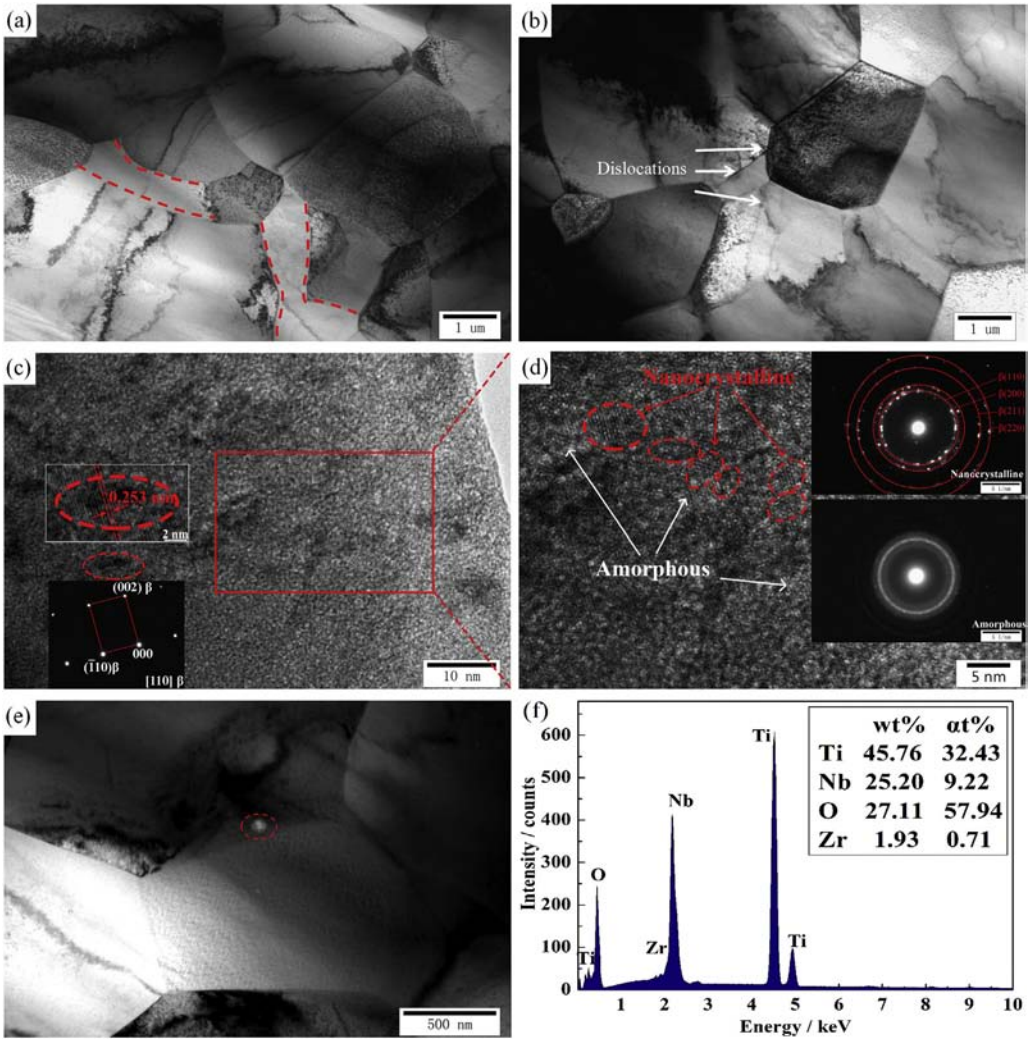

Fig. 5. TEM images of surface of stir zone in TiO_2 micro/nano-composite layers in R850D2: (a) recrystallized grains, (b) dislocations around the recrystallized grains, (c) HRTEM images of β phase with insets of SAED patterns, (d) magnified HRTEM images of nanocrystallines and amorphous phases in the region marked by red square in Fig. 5c with insets of SAED patterns, (e) the second phase, (f) element spectra for the second phase in Fig. 5e.

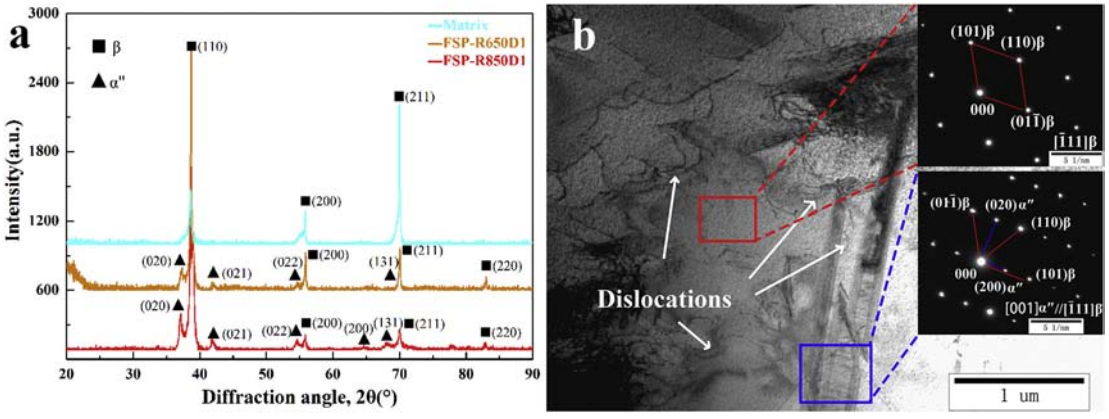

Fig. 6. XRD patterns and TEM image of α″ martensites: (a) XRD patterns of surface of the substrate and TiO_2 micro/nano-composite layers in R650D1 and R850D1, (b) TEM image of α″ martensites in surface of micro/nano-composite layers with insets of SAED patterns.

Fig. 7. EBSD maps: (a) orientation maps of surface of Ti-35Nb-2Ta-3Zr substrate and TiO_2 micro/nano-composite layers in R650D05 and R850D05. (b) recrystallization maps of surface of TiO_2 micro/nano-composite layers in R650D05 and R850D05. (c) distribution of grain size of the surface of TiO_2 micro/nano-composite layers in R650D05 and R850D05, (d) misorientation angle distribution of surface of TiO_2 micro/nano-composite layers in R650D05 and R850D05.

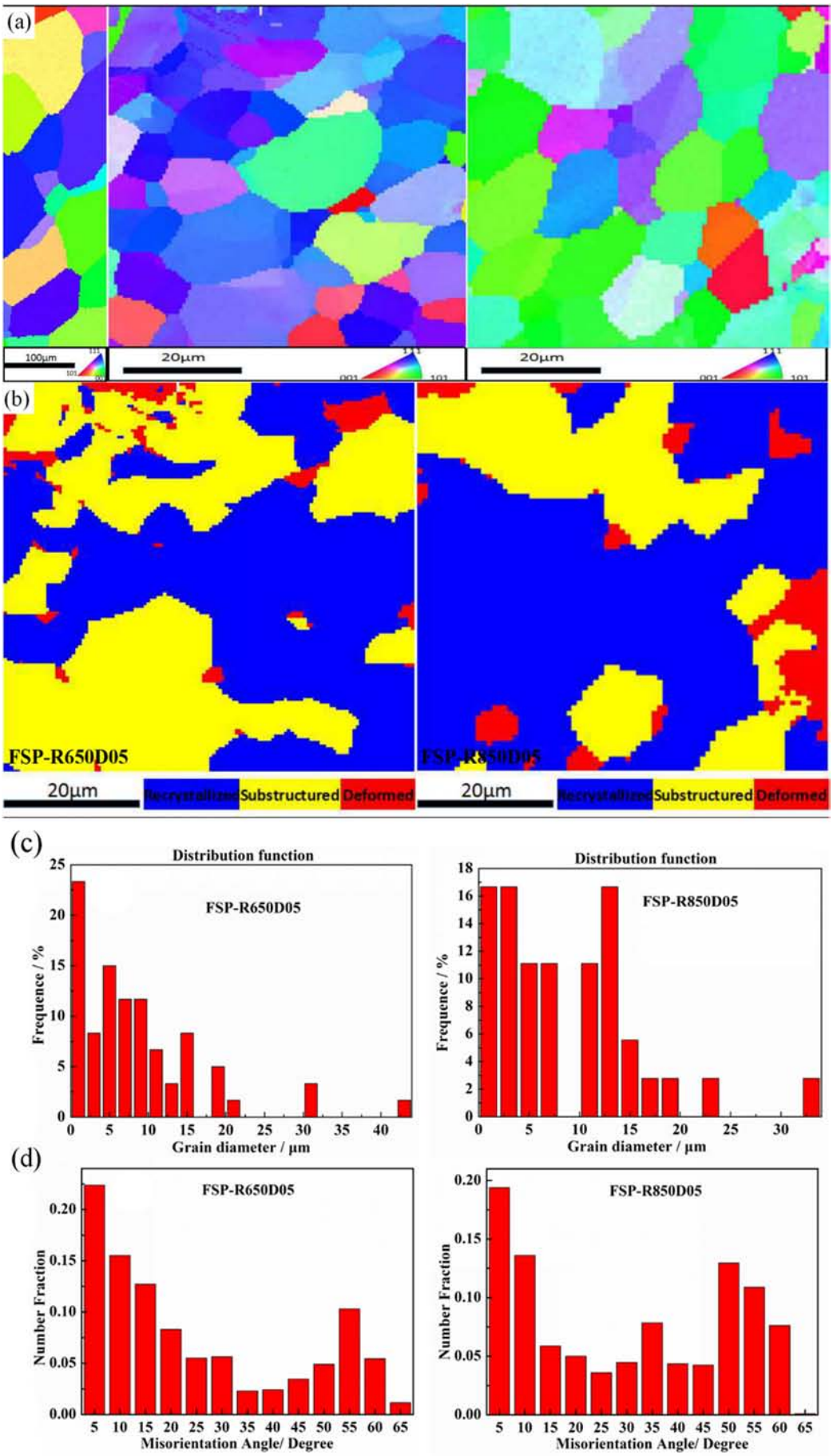
(a)
100μm
20μm
20μm
(b)
FSP-R650D05
FSP-R850D05
20μm
Recrystallized
Substructured
Deformed
20μm
Recrystallized
Substructured
Deformed
(c)
Distribution function
FSP-R650D05
Frequence / %
Grain diameter / μm
Distribution function
FSP-R850D05
Frequence / %
Grain diameter / μm
(d)
FSP-R650D05
Number Fraction
Misorientation Angle/ Degree
FSP-R850D05
Number Fraction
Misorientation Angle/ Degree

Table 2
The features of crystal structure of Ti-35Nb-2Ta-3Zr substrate, FSP-R650D05 and FSP-R850D05 groups by EBSD tests.

Groups	Grain Diameter/μm	HAGBs Fraction	Average misorientation angle/degree	Recrystallized fraction
Substrate	84.95	–	–	–
FSP-R650D05	8.54	62.12%	22.34	49.4%
FSP-R850D05	8.87	66.99%	27.66	63.8%

the R650D05 sample. Higher average misorientation angle of 27.66°and fraction of HAGBs of 66.99% are presented in the R850D05 sample, as recorded in Table 2, which means that more dynamic recrystallizations were induced by massive plastic deformation during the stir process. The relative mappings of recrystallized and deformed grains are displayed in Fig. 7b. It can be observed directly that R850D05 samples contain more recrystallized grains (63.8%) than R650D05 samples (49.4%). As it is known, the recrystallized grains result from dislocations and boundary slides, rooting in severe plastic deformation. More dislocations and migrations, which are embodied in higher misorientation angles, could bring about more recrystallized grains, especially at a high rotation speed during FSP. Furthermore, additive particles could effectively limit the growth of grains during dynamic recrystallization process, causing the refinement of grains. The anchoring and stabilization of particles accelerate dynamic recrystallization on the contrary.

3.2. Electrochemical corrosion

3.2.1. Potentiodynamic polarization curves

Fig. 8 shows potentiodynamic polarization curves of Ti-35Nb-2Ta-3Zr substrate and FSPed samples conducted in Hank's solution at 37 °C. The corrosion of β titanium alloy and its composites can be divided into four sections: the active, passive, re-active and secondary passive stages. The metal anode has lost electrons and dissolved in form of metal ions in the active stage of cathodic and anodic polarization, and gradually formed a stable passive film to resist corrosion, when the current maintain at a constant value with the increase of potential. When potential exceeds the threshold, the passive film breaks through and the current increases rapidly, entering the re-active stage. Afterwards, the growth rate of current decreases with the increase of potential, implying that secondary passivation occurs. As shown in Table 3, the corrosion potential (E_{corr}) of the Ti-35Nb-2Ta-3Zr substrate is −292.70 mV, higher than that of FSPed samples. However, as the most important kinetic parameter reflecting corrosion rate to evaluate corrosion behavior, a highest corrosion current density (125.08 nA/cm^2) was obtained by the substrate, which was fitted by

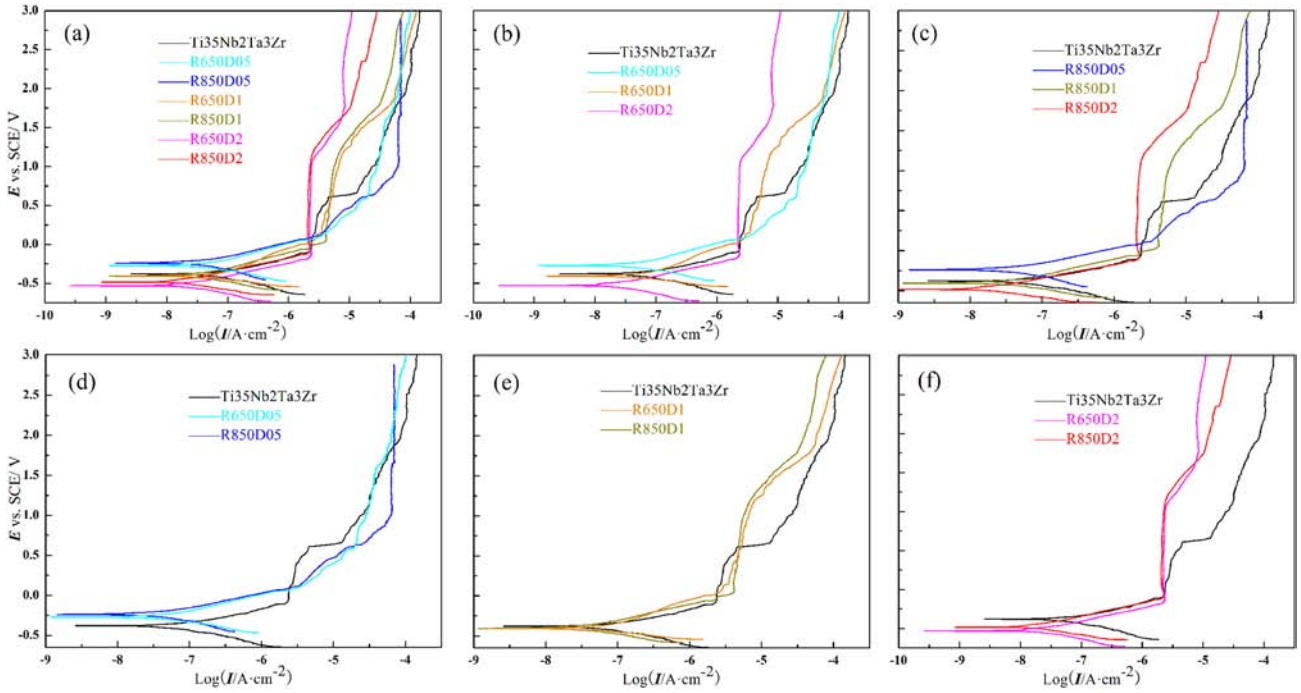

Fig. 8. Potentiodynamic polarization curves of the substrate and TiO_2 micro/nano-composite layers in Hank's solution.

Table 3
The potentiodynamic polarization results in Fig. 8 and values of the equivalent circuit elements used to fit the data of EIS in Fig. 9.

Groups	I_{corr} (nA/cm^2)	E_{corr} (mV) vs. SCE	R_{el} (Ω cm^2)	CPE1 (μΩ^{-1}cm^{-2}s^n)	n_1	R_1 (Ω cm^2)	R_2 (kΩ cm^2)	CPE2 (μΩ^{-1}cm^{-2}s^n)	n_2
Substrate	125.08 ± 44.23	−292.70 ± 85.51	18.81 ± 0.11	15.75 ± 0.21	0.86 ± 0	5848.33 ± 55.43	483.73 ± 47.55	32.16 ± 0.81	0.64 ± 0
R650D05	79.59 ± 31.01	−314.92 ± 84.85	9.87 ± 4.11	7.99 ± 4.67	0.97 ± 0.06	162.85 ± 61.27	611.57 ± 87.09	18.50 ± 10.67	0.74 ± 0.02
R650D1	62.92 ± 9.06	−410.92 ± 22.02	9.03 ± 3.19	12.69 ± 9.71	0.93 ± 0.09	94.63 ± 26.49	666 ± 76.05	16.93 ± 3.65	0.73 ± 0.09
R650D2	31.54 ± 3.31	−522.14 ± 19.35	12.10 ± 3.43	13.44 ± 9.36	0.97 ± 0.04	247.95 ± 142.38	1032.83 ± 147.56	14.55 ± 3.07	0.78 ± 0.02
R850D05	54.78 ± 6.87	−289.41 ± 49.16	16.82 ± 15.71	7.43 ± 3.30	0.98 ± 0.04	143.23 ± 17.12	707.43 ± 47.18	8.11 ± 2.07	0.81 ± 0.01
R850D1	42.64 ± 6.65	−408.90 ± 12.26	6.79 ± 0.09	5.56 ± 0.42	1 ± 0	88.76 ± 54.86	830.33 ± 34.29	17.59 ± 1.17	0.77 ± 0.01
R850D2	22.85 ± 3.27	−424.74 ± 49.10	6.72 ± 5.48	8.59 ± 2.14	0.95 ± 0.08	305.7 ± 94.21	1346 ± 21.70	11.87 ± 7.87	0.80 ± 0.04

R_{el} denotes the resistance of the electrolyte, while, R1 and R2 represent the resistances of outer and inner layers. CPE1 and CPE2 are the capacitances of the outer and inner layers respectively. CPE is a constant phase element to describe a non-ideal capacitive behavior. The impedance is defined as $Z_{CPE} = [C(j\omega)^n]^{-1}$, where j is imaginary part, ω is the frequency and n is affected by surface roughness and inhomogeneity.

Tafel plot. At the same rotation speed, I_{corr} decreases with the increasing amount of TiO_2 added, as shown in Table 3 (79.59 nA/cm^2, 62.92 nA/cm^2, 31.54 nA/cm^2 respectively for R650D05, R650D1 and R650D2). Similarly, the average values are 54.78 nA/cm^2, 42.64 nA/cm^2, and 22.85 nA/cm^2 at 850 rpm speed. Compared with the substrate, I_{corr} of the material with the most TiO_2 added reduces by 5 times, indicating that corrosion resistance has been further improved by TiO_2 micro/nano-composite layer. Meanwhile, with the same addition depth, higher rotation speed appears conducive to better corrosion resistance, according to the lower I_{corr} and higher E_{corr} by contrast. As shown in Fig. 8, the range of passive region widens, especially when addition depths are 1 mm and 2 mm at the two rotation speeds, implying the formation of a more stable and compact passive film. Though the values of E_{corr} have declined with the increase of amount of TiO_2 added, border ranges of passive stage and lower values of I_{corr} were obtained by greater amount of TiO_2 particles, showing decreased corrosion rate. Thus it can be said that the increasing rotation speed and amount of TiO_2 added have indeed improved corrosion resistance of the material in simulated human body environment.

3.2.2. Electrochemical impedance spectroscopy

As presented in Fig. 9, the electrochemical impedance spectroscopy of samples was conducted at OCP in Hank's solution. Fig. 9a is the Nyquist plot based on the data. Obviously, the substrate possesses a smallest radius and the radiuses of FSPed samples enlarge with the increase of rotation speed and amount of TiO_2 added, indicating that better corrosion resistance properties are obtained [42]. An equivalent circuit model composed of resistances and capacitances has been established to fit the EIS data, illustrated in the inset of Fig. 9a and the same model was used in the similar researches [43–47]. The fitting parameters are presented in Table 3, and the chi-square values are between 10^{-3} and 10^{-4}. The substrate reveals a highest R_1 of about 5850 Ω cm^2, much larger than those of FSPed samples, implying a thicker outer layer obtained on the substrate. However, the value of R_2 of the substrate is the lowest among all the samples. Considering the value of R_2 is much larger than R_1 for all the samples, without doubt inner layers play the dominant role of corrosion resistance as barriers. The formation of porous loosened outer layers should account for the low values of R_1 of FSPed samples. R_2 of the sample R850D2 has risen by three times compared with that of the substrate, from 484 kΩ cm^2 up to 1346 kΩ cm^2. Moreover, with the increase of rotation speed and amount of TiO_2 added, higher values of R_2 have been acquired, expressing better corrosion resistance properties of micro/nano-composite layers processed by FSP. At the 650 rpm speed, the values of R_1 are similar (about 170 Ω cm^2) and R_2 are 611.57 kΩ cm^2, 666 kΩ cm^2 and 1032.83 kΩ cm^2 corresponding to 0.5, 1 and 2 mm additive particles depth. Similarly, at the 850 rpm speed, the values of R_1 approximate the values at 650 rpm speed, and R_2 are 707.43 kΩ cm^2, 830.33 kΩ cm^2 and 1346 kΩ cm^2 respectively. Compared with the substrate, larger n1 (near 1) and n2 (about 0.8) are obtained in the FSPed samples, indicating a trend of electrochemical behavior like an ideal capacitor. Besides, higher rotation speed improves slightly the value of n2 from 0.75 to nearly 0.8. The capacitances of outer porous layer (CPE1) and inner barrier layer (CPE2) of FSPed samples decrease in comparison with the substrate, which are related to surface topography and thickness of passive film [48,49], and a lower capacitance may be associated to a better electrochemical corrosion behavior [50]. Compared with 650 rpm rotation speed, similar decreasing tendency could be observed in the values of CPE1 (from 11 to 7 $\mu\Omega^{-1}cm^{-2}s^n$) and CPE2 (from 17 to 12.5 $\mu\Omega^{-1}cm^{-2}s^n$) at 850 rpm speed.

Bode diagrams of the substrate and FSPed samples are illustrated in Fig. 9b and c. The Bode modulus plots reveal the same linear region at the middle and low frequencies, indicating a similar mostly capacitive behavior for the untreated and FSPed samples, in agreement with the analyses of polarization curves. The phase plots of the substrate show two peaks, as well as, merged broad peaks for TiO_2 micro/nano-composite layers can also be seen in Fig. 9b and c induced by cumulative capacitive effects. This indicates two time constants during corrosion, due to the formation of a compact passive film on surface. At the 650 rpm rotation speed, the peak angle of R650D2 approaches 79.58°, higher than that of R650D05 (75.26°) and R650D1 (74.42°). In contrast, the peak angle of the substrate is 70.94°, obviously lower than that of the treated samples, indicating a less capacitive behavior. At the 850 rpm speed, the peak angles are 81.07°, 78.10° and 80.54° for 0.5, 1 and 2 mm respectively. In general, higher peak angles are obtained at a higher rotation speed, implying the formation of a highly stable passive film.

3.2.3. AFM results

Fig. 10 shows morphological images collected in the Hank's solution at OCP and after potentiodynamic polarization respectively. As illustrated in Fig. 10a, the topography of the substrate after polarization presents as waved hills with little fluctuations, of which the R_q (root-mean-square roughness) is only 3.67 nm. However, obvious changes could be directly seen in morphological images of TiO_2 micro/nano-composite layers after corrosion. In Fig. 10b, serried needlelike surfaces accompanied with thick oxide clusters are observed for R850D05 at OCP, which possesses a lowest R_q value of 3.34 nm, indicating the homogeneous growth and formation of a stable passive film. Analogously, in Fig. 10c and d, the surfaces of R650D1 and R650D2 after polarization seem rough with dispersive short embossments, of which the R_q values are 16.5 nm and 16 nm respectively. This could be attributed to the consumption of original dense needlelike layers by electrochemical corrosion. Compared with the original surfaces of composite layers at OCP, little changes occurred on the surfaces of R850D1 and R850D2 after polarization in Fig. 10e and f, of which R_q values are 7.2 nm and 3.18 nm, demonstrating better corrosion resistance at a higher rotation speed. The local current maps for the substrate and R650D05 after polarization are presented in Fig. 10g and h respectively. Some white regions can be noticed in the map of the substrate, which denote the maximum magnitude of current. This indicates that breakdown of passive film on the substrate has occurred. However, uniform current distribution can be seen in the maps of R650D05, denoting the formation of a more stable homogeneous passive film on micro/nano-composite layers.

3.2.4. Composition and depth profiles of the passive films conducted by XPS

The chemical components of the oxide films formed on the substrate and TiO_2 micro/nano-composite layers conducted by XPS are illustrated in Fig. 11. The samples were oxidized for 1.5 h in Hanks solution at 0.5 V, which is located in the first passive stage of polarization curves, to obtain stable passive oxide films. It can be noticed that the oxide films mainly consist of titanium, niobium, tantalum, zirconium, carbon and their oxides in Fig. 11a. The existence of carbon results from the contact with air. The peak of Ti $2p_{3/2}$ is located at 458.7 eV in Fig. 11b, indicating the major component of oxide films is TiO_2. Besides, titanium and other related oxides can be observed including TiO and Ti_2O_3. The content ratios of titanium and oxides of the substrate and treated samples are presented in Table 4. TiO_2 prevails in the oxide films, and the content increases in FSPed samples in comparison with the substrate. Moreover, the proportion of TiO_2 rises with the increase of rotation speed and amount of TiO_2 added, and the low content of sub-oxides presents the opposite behavior, denoting the occurrence of more complete oxidation and the formation of more stable passive films. The peak of Nb $3d_{5/2}$ is located at 207.4 eV, signifying Nb_2O_5 as the main oxide in Fig. 11c. No sub-oxides could be noticed on the surface of R850D1, indicating complete oxidation of niobium. The position of Ta $4f_{7/2}$ peak is seated at 22.8 and 26 eV, representing tantalum and its oxides in Fig. 11d. The sub-oxides are defined as TaO_x ($1 < x < 2$), due to the similar binging energy of TaO and TaO_2. Different from other alloying elements, tantalum and the sub-oxides prevail over Ta_2O_5. In Fig. 11e, the main peak of Zr $3d_{5/2}$ is at 182.4 eV, which accounts for preponderant ZrO_2. Meanwhile, very small amount of zirconium could be found.

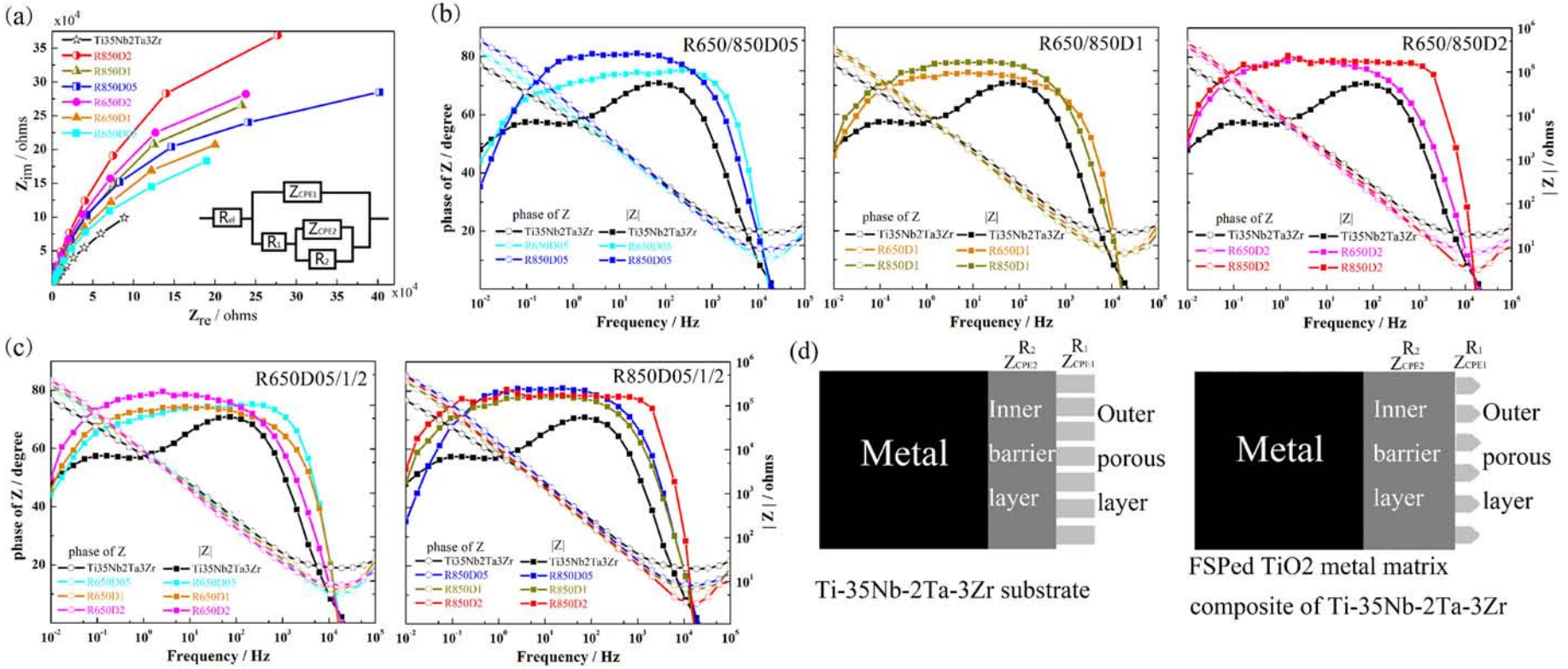

Fig. 9. EIS pattern of the substrate and TiO_2 micro/nano-composite layers in Hank's solution: (a) Nyquist diagram with equivalent circuit, (b) Bode diagrams of TiO_2 micro/nano-composite layers at the different rotation speed with the same amount of TiO_2 added, (c) Bode diagrams of TiO_2 micro/nano-composite layers at the same rotation speed with the different amount of TiO_2 added, (d) related schematic diagrams of the substrate and TiO_2 micro/nano-composite layers.

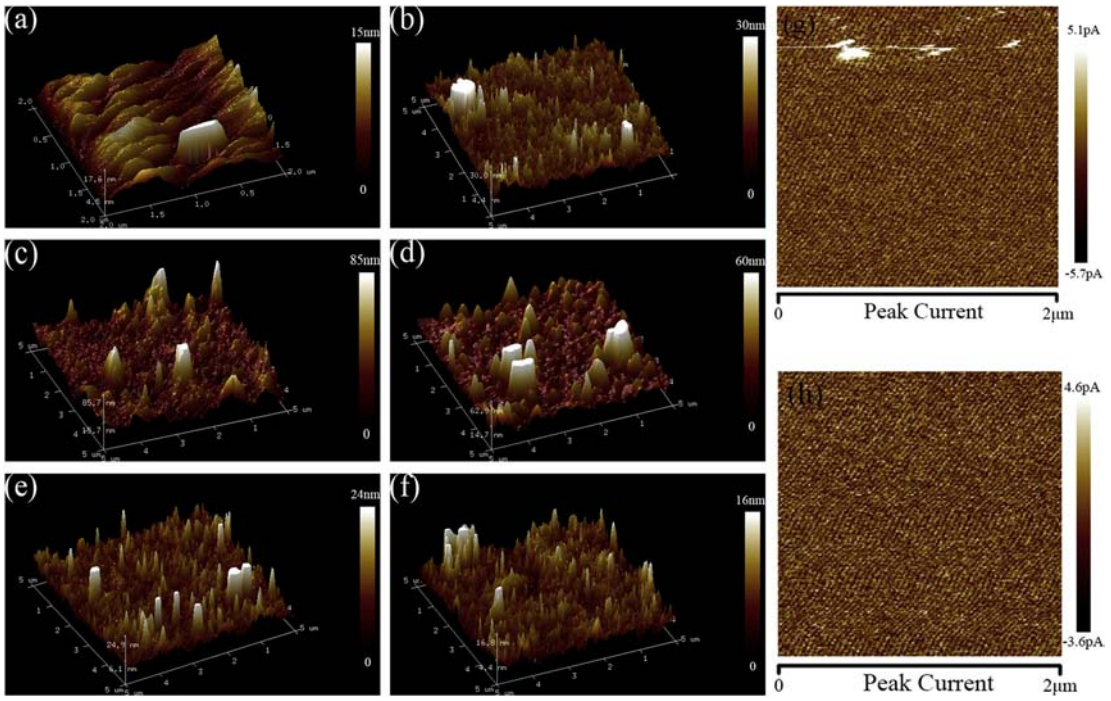

Fig. 10. AFM images of morphology structure: (a) surface of the substrate after polarization, (b) surface of R850D05 at OCP, (c) surface of R650D1 after polarization, (d) surface of R650D2 after polarization, (e) surface of R850D1 after polarization and (f) surface of R850D2 after polarization, (g) local current maps of surface of the substrate, (h) local current maps of surface of R650D05.

In-depth composition and thickness of the surface layers of the substrate and R850D1 were investigated by XPS depth profiles in Fig. 11f and g. The changes in main elements of titanium, niobium and oxygen with depth are recorded in the curves. It can be noticed that the content of oxygen decreases with the sputter process and the contrary situation has taken place in titanium and niobium, denoting the decrease of metallic oxides of high valence and the increase of sub-oxides and metal. This could be attributed to oxygen migration from surface to the depth. To facilitate the measurement, the thickness of the surface oxide layer is defined as the arithmetic product of sputtering rate of 2 nm/min related to the SiO_2 standard and the sputtering time of the decrease of oxygen content from surface to half initial quantity [51]. The estimated time of the substrate is from the beginning (69.5%) to half (35%), as 1200 s, while the time of R850D1 is from 75% to 38%, as 1800 s. The apparent increase of thickness of R850D1 for 60 nm, compared with the substrate for 40 nm, indicating a better corrosion resistance of TiO_2 micro/nano-composite layers.

4. Discussion

4.1. Formation of a compact stable passive film on surface of TiO_2 micro-nanocomposite layers

Corrosion resistance of a material mostly depends on the passive films formed on the surface, which inhibit further corrosion from surface to deep [47]. The passive current density and the breakdown potential are usually used to evaluate the characteristic of passive films. As shown in Fig. 8, excellent passive current density was obtained in the TiO_2 micro/nano-composite layers, especially when most TiO_2 particles were added before FSP. The low passive current density (about 2.1 $\mu A/cm^2$) in R850D2 indicates an extremely weak electrical conductivity of passive films. Meanwhile, the highest breakdown potential for about 1.1 V in R650D2 and R850D2 samples denotes wider range of passivation, facilitating stability of oxide films. Hence, TiO_2 micro/nano-composite layers are conducive to the formation of a compact stable passive film. Besides, lower corrosion current density was measured in the TiO_2 micro/nano-composite layers in comparison with the substrate, and the decrease is more remarkable with the increase of rotation speed and amount of TiO_2 particles added. However, in terms of corrosion potential, the inverse behavior displayed with the increase of amount of TiO_2 particles, which is a thermodynamic parameter representing the potential of corrosion and could not provide an objective evaluation of corrosion because of many influence factors. The phenomenon could be related to the porous characterization of micro/nano-composite layers. It is considered that lower oxygen content inside the pores could lead to lower exchange current density of oxygen reduction reaction, causing more polarization of cathodic reaction [52]. Similar results were conducted by Zhang and El-Lateef [31,53]. As presented in Fig. 9, besides larger radius of capacitive arc in the Nyquist diagram and higher peak angles in the Bode diagram, TiO_2 micro/nano-composite layers reveal wider frequency range of peak angle and higher phase angles at low frequency of 0.01 Hz. Moreover, the promotion appears more obvious with the increase of rotation speed and amount of TiO_2. Thus, it is reasonable to believe that TiO_2 micro/nano-composite layers contribute to corrosion resistance, especially for higher rotation speed and larger amount of TiO_2.

4.2. Reasons of advanced corrosion resistance

As the most significant factor, the optimization of passive films mainly depends on the following three points: (i) the constituents of oxide films; (ii) the thickness of oxide films; (iii) structural characteristics of oxide films.

Metallic oxides of high valence in passive films can lead to the reduction of oxygen vacancies, inhibiting the diffusion of oxygen through the barrier layers with the thickening of oxide films [54]. Thereby, some sub-oxides tend to form at film/metal interface because of the blocking oxygen effect of passive films [55]. More TiO_2 has formed on surface of oxide films of micro/nano-composite layers in comparison with the substrate, and higher rotation speed and more added TiO_2 particles have promoted the phenomenon. Higher proportions of metallic oxides

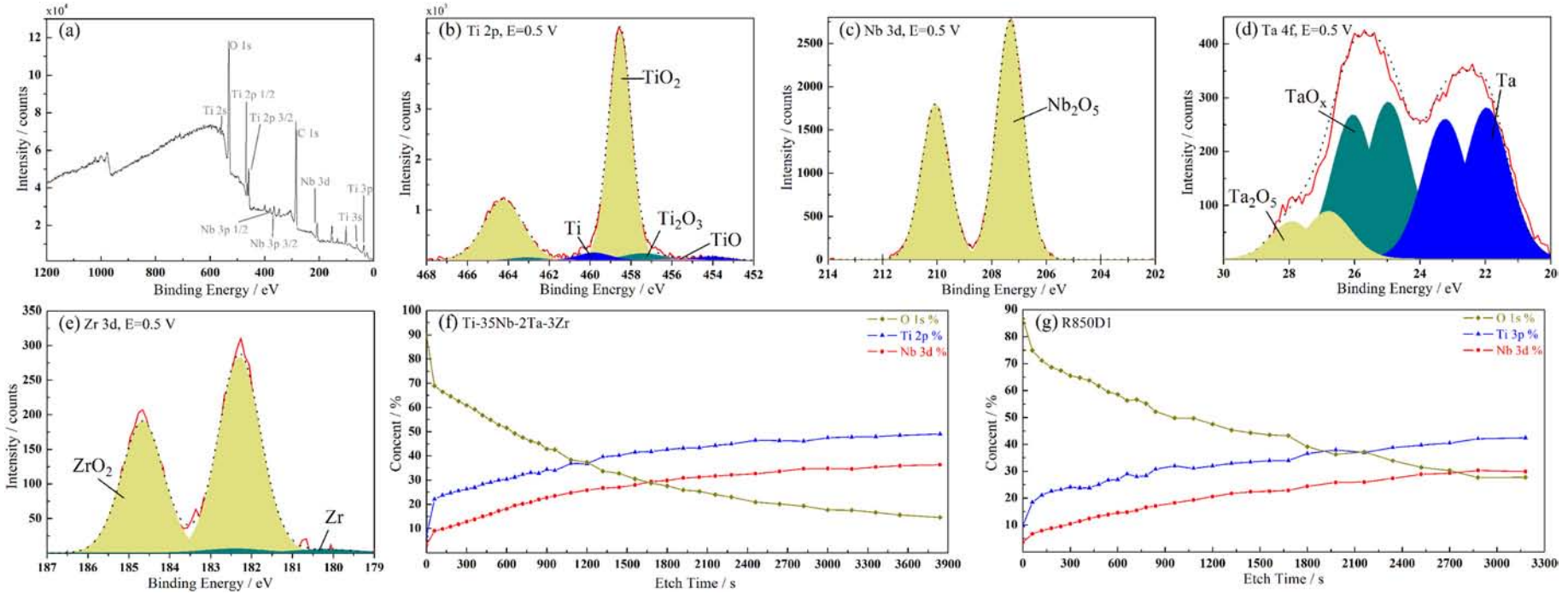

Fig. 11. XPS analysis: (a) general spectra on the surface of R850D05, (b) deconvoluted XPS spectra of Ti on the surface of R850D05, (c) deconvoluted XPS spectra of Nb on the surface of R850D05, (d) deconvoluted XPS spectra of Ta on the surface of R850D05, (e) deconvoluted XPS spectra of Zr on the surface of R850D05, (f) depth profiles of the substrate, (g) depth profiles of R850D05.

Table 4
The content proportions of titanium and oxides in Fig. 11b, and the estimated thickness of surface layers of the substrate and R850D1 conducted by XPS sputter depth profiles in Fig. 11f and g.

Groups	TiO_2 (%)	Ti_2O_3 (%)	TiO (%)	Ti (%)	Thickness (nm)
Substrate	78.29	12.45	2.65	6.61	40
R650D1	86.85	5.11	1.91	6.13	–
R650D2	89.46	4.46	0.96	5.12	–
R850D1	89.55	4.42	1.84	4.19	60
R850D2	90.07	4.48	0.86	4.59	–

of high valence indicate less penetration of oxygen and better protectiveness of passive films.

When the argon ion beams bombard deep, as illustrated in Fig. 11f and g, the ratio of titanium and oxygen elements decreases from 2:1 to 1:1 or even lower, representing the changes of oxide composition from TiO_2 to the compound of TiO_2, Ti_2O_3, TiO and Ti, which indicates formation of more sub-oxides of titanium in the deep. According to the definition, passive oxide films should consist of titanium oxides even if it is of low valence states, that is to say, the ratio of titanium and oxygen elements should be >1:1. Moreover, sputtering time spent on the defined oxide films and dropping rate of oxygen in the modified sample are distinctly superior to the substrate, demonstrating the formation of a thicker homogeneous compact film. The estimated thickness of the oxide film formed on surface of TiO_2 micro/nano-composite layer increased by 50% compared with the substrate, confirming the above standpoints.

The AFM images provide the visualized information of morphology changes of micro/nano-composite layers and the substrate after electrochemical corrosion. Nano-scale needlelike porous surface structure of TiO_2 micro/nano-composite layers was discovered in a stabled state at OCP, and little changed after polarization especially with higher rotation speed and more TiO_2 particles added, indicating better corrosion resistance. Meanwhile, compared with the substrate, passive films formed on surface of micro/nano-composite layers without current breakdown appear more compact and stable. Together with EIS parameters in Table 3, related schematic diagrams were made to expound mechanism of promoted corrosion resistance in Fig. 9d. Combined with morphology structure of the substrate, a thicker porous outer layer like waved hills was formed, accompanied with a thinner inner barrier layer. With regard to TiO_2 micro/nano-composite layers, a thicker and compact barrier layer was coupled with a thin serried needlelike porous outer layer.

4.3. Effect of optimized microstructure on the passive films in surface of TiO_2 micro/nano-composite layers

The differences between passive films on modified samples and the substrate mainly attribute to friction stir processing and additive TiO_2 particles. During the one-pass FSP procedure, grain refinement promoted the formation of micro/nano-sized β titanium and nanocrystallines with numerous grain boundaries of high energy. The migration of boundaries usually takes place in high stacking fault energy (SFE) metals with severe deformation and thermal energy [56]. Dynamic recrystallization and related HAGBs could be ascribed to the boundary migration and sustaining dislocation absorption on low-angle grain boundaries (LAGBs). Similar conclusions were obtained by Li and other scholars [57,58]. These massive boundaries improve activity and accelerate diffusion of electron to supply more sites for nucleation of oxide films on the modified metal surface, which leads to the rapid formation of passive films and favorable adherence between surface and oxide films [59]. Besides, a large number of dislocations occurred especially around grain boundaries due to severe plastic deformation generating during stir, as seen in Fig. 4 and Fig. 5. These dislocations and grain boundaries have more specific surface area and surface free energy to form oxidation channels [60]. The uniform distribution of grains boundaries could facilitate balance of Gibbs free energy between grain boundaries and grain internal so as to decrease local corrosion [61]. Oxide films of different geometry can better fit superficial structures on account of the plenty of grain boundaries. Besides, other factors such as martensite and oxygen distribution should also be taken into account for corrosion resistance improvement. It has been reported that oxygen atoms expand the surrounding atoms (Ti and Nb), and promote the shuffling and shearing in α″ martensite [62]. These shuffling and extrusion could induce more nucleation of oxide and contribute to electron diffusion. Uniformly dispersive oxygen in micro/nano-composite layers is beneficial to fast development of oxide films because of less required accumulation of oxygen when corrosion just happens. Meanwhile, the reduction of oxygen vacancies could be induced by occupied oxygen atoms and metal ions of high valences [53].

It has been reported that reinforcement particles can inhibit grain growth when the size and spacing of particles is <0.1 mm and 1.5 mm respectively [63]. Mutual dislocations and slips facilitate anchoring and stabilization of particles. On one hand, massive dislocations and grain refinement could restrict the accumulation of particles. On the other hand, additive TiO_2 particles play a role in limiting the growth of grains during dynamic recrystallization process. As main component of passive films, TiO_2 are in favor of corrosion resistance in theory. Furthermore, needlelike porous surface might be beneficial to adsorb osteogenesis factors and create a micromechanical anchorage with bone interlocking [64]. The modified surface and corrosion resistance of TiO_2 micro/nano-composite layers provide new ideas for medical implants.

5. Conclusions

The microstructures and corrosion resistance of TiO_2 micro/nano-composite layers on Ti-35Nb-2Ta-3Zr by friction stir processing have been revealed. The influences of different FSP parameters (rotation speed and amount of TiO_2 particles added) were discovered and the relationship between microstructures and corrosion resistance were discussed in detail. The main conclusions are enumerated as follows:

(1) Different from coarse grains in the Ti-35Nb-2Ta-3Zr substrate, surface of TiO_2 micro/nano-composite layers presents massive uniform and finer equiaxed β grains (around 8 μm) with homogeneous dispersive oxygen. Besides β phases, nanocrystallines and amorphous phases were discovered.
(2) Massive dislocations and deformation were formed during FSP with high fraction of high angle grain boundaries (HAGBs), implying occurrence of dynamic recrystallization (DRX). Needle-shaped α″ martensites were discovered in surface of stir zones, which were attributed to severe deformation and thermal energy. Higher rotation speed facilitated more formation of dynamic recrystallization and α″ martensites.
(3) Compared with the substrate, TiO_2 micro/nano-composite layers revealed lower corrosion current density (22.85 nA/cm^2) and passive current density (about 2.1 $\mu A/cm^2$) with widen passive range. Besides, with increase of rotation speed and amount of TiO_2 added, composite layers possessed larger resistance of barrier layers (1346 $k\Omega\ cm^2$), higher peak phase angles (81.07°) and widen peak angle range. Different from passive films of the substrate, more dense and compact inner barrier layers and more porous outer layers were formed on surface of composite layers.
(4) More titanium oxides of high valence states were discovered in the TiO_2 micro/nano-composite layers and the behavior appeared more obvious with increase of rotation speed and amount of TiO_2 added. The estimated thickness of oxide film on micro/nano-composite layers was 60 nm in comparison with the substrate of 40 nm by depth profiles.
(5) Different from morphology structure of the substrate like waved hills, dense needlelike surface structure was observed on surface of TiO_2 micro/nano-composite layers after polarization. Compared

with morphology structure at OCP, fewer changes occurred after polarization with increase of rotation speed and amount of TiO_2 particles added. In addition, composite layers showed a more compact passive film without current breakdown region in the local current maps.

Acknowledgements

This work was financially supported by National Science Foundation (grant number 51302168, 51674167, 81828007), Medical Engineering Cross Research Foundation of Shanghai Jiao Tong University (grant number YG2014MS02) and State Key Laboratory of Powder Metallurgy, Central South University, Changsha, China.

Credit author statement

Y. Fu, L. Wang and K. Wang performed the concept of the study and provided funding support. L. Zhang and W. Lu provided experimental materials and processing technology support. Z. Ding and Z. Yang conducted the part of microstructure experiments. H. Gu conducted the part of electrochemical property experiments and performed data analysis. W. Yu and W. Zhang performed overall data analysis. H. Gu, Y. Fu, L. Wang and K. Wang performed the constructive discussions. H. Gu, Z. Ding and Z. Yang drafted the manuscript. W. Yu and W. Zhang reviewed the manuscript. H. Gu, Y. Fu, L. Wang and K. Wang integrated the suggestions of all authors and finished the paper.

References

[1] C.D. Rabadia, Y.J. Liu, S.F. Jawed, L. Wang, Y.H. Li, X.H. Zhang, T.B. Sercombe, H. Sun, L.C. Zhang, Improved deformation behavior in Ti-Zr-Fe-Mn alloys comprising the C14 type laves and β phases, Mater. Des. 160 (2018) 1059–1070.
[2] C.D. Rabadia, Y.J. Liu, L. Wang, H. Sun, L.C. Zhang, Laves phase precipitation in Ti-Zr-Fe-Cr alloys with high strength and large plasticity, Mater. Des. 154 (2018) 228–238.
[3] X.Y. Yang, C.R. Hutchinson, Corrosion-Wear of β-Ti alloy TMZF (Ti-12Mo-6Zr-2Fe) in simulated body fluid, Acta Biomater. 42 (2016) 429–439.
[4] C. Vasilescu, S.I. Drob, J.M.C. Moreno, P. Osiceanu, M. Popa, E. Vasilescu, Long-term corrosion resistance of new Ti–Ta–Zr alloy in simulated physiological fluids by electrochemical and surface analysis methods, Corros. Sci. 93 (2015) 310–323.
[5] J.M. Hernández-López, A. Conde, J.D. Damborenea, M.A. Arenas, Correlation of the nanostructure of the anodic layers fabricated on Ti13Nb13Zr with the electrochemical impedance response, Corros. Sci. 94 (2015) 61–69.
[6] V.S. Saji, C.C. Han, Electrochemical corrosion behaviour of nanotubular Ti–13Nb–13Zr alloy in Ringer's solution, Corros. Sci. 51 (2009) 1658–1663.
[7] C. Xia, Z. Zhang, Z. Feng, B. Pan, X. Zhang, M. Ma, Effect of zirconium content on the microstructure and corrosion behavior of Ti-6Al-4V- x Zr alloys, Corros. Sci. 112 (2016) 687–695.
[8] H. Jha, R. Hahn, P. Schmuki, Ultrafast oxide nanotube formation on TiNb, TiZr and TiTa alloys by rapid breakdown anodization, Electrochim. Acta 55 (2010) 8883–8887.
[9] L. Wang, W. Lu, J. Qin, F. Zhang, D. Zhang, Microstructure and mechanical properties of cold-rolled TiNbTaZr biomedical β titanium alloy, Mater. Sci. Eng. A 490 (2008) 421–426.
[10] A. Mazare, G. Totea, C. Burnei, P. Schmuki, I. Demetrescu, D. Ionita, Corrosion, antibacterial activity and haemocompatibility of TiO2, nanotubes as a function of their annealing temperature, Corros. Sci. 103 (2016) 215–222.
[11] M. Long, H.J. Rack, Titanium alloys in total joint replacement—a materials science perspective, Biomaterials 19 (1998) 1621–1639.
[12] I. Cvijović-Alagić, Z. Cvijović, S. Mitrović, V. Panić, M. Rakin, Wear and corrosion behaviour of Ti–13Nb–13Zr and Ti–6Al–4V alloys in simulated physiological solution, Corros. Sci. 53 (2011) 796–808.
[13] L.F. Hu, J. Li, Y.F. Tao, Y.H. Lv, Corrosion behaviors of TiNi/Ti2Ni matrix coatings in the environment rich in Cl ions, Surf. Coat. Technol. 311 (2017) 295–306.
[14] F. El-Taib Heakal, A.A. Ghoneim, A.S. Mogoda, Kh. Awad, Electrochemical behaviour of Ti–6Al–4V alloy and Ti in azide and halide solutions, Corros. Sci. 53 (2011) 2728–2737.
[15] N.T.C. Oliveira, A.C. Guastaldi, Electrochemical behavior of Ti–Mo alloys applied as biomaterial, Corros. Sci. 50 (2008) 938–945.
[16] X.P. Wang, F.T. Kong, B.Q. Han, Y.Y. Chen, Electrochemical corrosion and bioactivity of Ti-Nb-Sn-hydroxyapatite composites fabricated by pulse current activated sintering, J. Mech. Behav. Biomed. Mater. 75 (2017) 222–227.
[17] C. Prakash, M. Uddin, Surface modification of β-phase Ti implant by hydroaxyapatite mixed electric discharge machining to enhance the corrosion resistance and in-vitro bioactivity, Surf. Coat. Technol. 326 (2017) 134–145.
[18] I.M. Pohrelyuk, V.M. Fedirko, O.V. Tkachuk, R.V. Proskurnyak, Corrosion resistance of Ti–6Al–4V alloy with nitride coatings in Ringer's solution, Corros. Sci. 66 (2013) 392–398.
[19] G. Bolat, J. Izquierdo, T. Gloriant, R. Chelariu, D. Mareci, R.M. Souto, Investigation of processing effects on the corrosion resistance of Ti20Mo alloy in saline solutions, Corros. Sci. 98 (2015) 170–179.
[20] L.C. Zhang, Y. Liu, S. Li, Y. Hao, Additive manufacturing of titanium alloys by electron beam melting: a review, Adv. Eng. Mater. 20 (2018) 1700842.
[21] Y. Lv, Y. Ding, Y. Han, L.C. Zhang, L. Wang, W. Lu, Strengthening mechanism of friction stir processed and post heat treated NiAl bronze alloy: effect of rotation rates, Mater. Sci. Eng. A 685 (2016) 439–446.
[22] D.R. Ni, B.L. Xiao, Z.Y. Ma, Y.X. Qiao, Y.G. Zheng, Corrosion properties of friction–stir processed cast NiAl bronze, Corros. Sci. 52 (2010) 1610–1617.
[23] A. Fattah-Alhosseini, M. Vakili-Azghandi, M. Sheikhi, M.K. Keshavarz, Passive and electrochemical response of friction stir processed pure titanium, J. Alloys Compd. 704 (2017) 499–508.
[24] X. Liu, P.K. Chu, C. Ding, Surface modification of titanium, titanium alloys, and related materials for biomedical applications, Mater. Sci. Eng. R 47 (2004) 49–121.
[25] M. Mirak, M. Alizadeh, M.N. Ashtiani, Characterization, mechanical properties and corrosion resistance of biocompatible Zn-HA/TiO2 nanocomposite coatings, J. Mech. Behav. Biomed. Mater. 62 (2016) 282–290.
[26] S.Z. Khalajabadi, N. Ahmad, S. Izman, A.B.H. Abu, W. Halder, M.R.A. Kadlr, In vitro, biodegradation, electrochemical corrosion evaluations and mechanical properties of an Mg/HA/TiO2, nanocomposite for biomedical applications, J. Alloys Compd. 696 (2017) 768–781.
[27] K.V.S. Murthy, D.P. Girish, R. Keshavamurthy, T. Varol, P.G. Koppad, Mechanical and thermal properties of AA7075/TiO2 /Fly ash hybrid composites obtained by hot forging, Prog. Nat. Sci. 27 (2017) 474–481.
[28] X. He, G. Zhang, X. Wang, R. Hang, X. Huang, L. Qin, B. Tang, X. Zhang, Biocompatibility, corrosion resistance and antibacterial activity of TiO2 /CuO coating on titanium, Ceram. Int. 43 (2017) 16185–16195.
[29] Y.Y. Guo, M.Q. Cheng, D.S. Chen, X.B. Xue, X.L. Zhang, In vitro corrosion resistance and cytotoxicity of novel TiNbTaZr alloy, Trans. Nonferrous Met. Soc. China 22 (2012) 175–180.
[30] L. Wang, L. Xie, Y. Lv, L.C. Zhang, L. Chen, Q. Meng, J. Qu, D. Zhang, W. Lu, Microstructure evolution and superelastic behavior in Ti-35Nb-2Ta-3Zr alloy processed by friction stir processing, Acta Mater. 131 (2017) 499–510.
[31] C. Zhang, Z. Ding, L. Xie, L.C. Zhang, L. Wu, Y. Fu, L. Wang, W. Lu, Electrochemical and in vitro behavior of the nanosized composites of Ti-6Al-4V and TiO2 fabricated by friction stir process, Appl. Surf. Sci. 423 (2017) 331–339.
[32] Z. Ding, C. Zhang, L. Xie, L.C. Zhang, L. Wang, W. Lu, Effects of friction stir processing on the phase transformation and microstructure of TiO2-compounded Ti-6Al-4V alloy, Metall. Mater. Trans. A 47 (2016) 5675–5679.
[33] Z. Yang, H. Gu, G. Sha, W. Lu, W. Yu, W. Zhang, Y. Fu, K. Wang, L. Wang, TC4/Ag metal matrix nanocomposites modified by friction stir processing: surface characterization, antibacterial property, and cytotoxicity in vitro, ACS Appl. Mater. Interfaces 10 (2018) 41155–41166.
[34] A. Fattahalhosseini, O. Imantalab, G. Ansari, The role of grain refinement and film formation potential on the electrochemical behavior of commercial pure titanium in Hank's physiological solution, Mater. Sci. Eng. C 71 (2017) 827–834.
[35] R. Rajeshkumar, V. Udhayabanu, A. Srinivasan, Microstructural evolution in ultrafine grained Al-graphite composite synthesized via combined use of ultrasonic treatment and friction stir processing, J. Alloys Compd. 726 (2017) 358–366.
[36] P.E. Batson, Spatial resolution in electron energy loss spectroscopy, Ultramicroscopy. 47 (1992) 133–144.
[37] Y. Lv, Z. Ding, J. Xue, G. Sha, E. Lu, L. Wang, W. Lu, C. Su, L.C. Zhang, Deformation mechanisms in surface nano-crystallization of low elastic modulus Ti6Al4V/Zn composite during severe plastic deformation, Scr. Mater. 157 (2018) 142–147.
[38] R. Ran, Y. Liu, L. Wang, E. Lu, L. Xie, W. Lu, K. Wang, L. Zhang, α″ Martensite and amorphous phase transformation mechanism in TiNbTaZr alloy incorporated with TiO2 particles during friction stir processing, Metall. Mater. Trans. A. 49 (2018) 1986–1991.
[39] T.H. Ahn, C.S. Oh, D.H. Kim, K.H. Oh, H. Bei, E.P. George, H.N. Han, Investigation of strain-induced martensitic transformation in metastable austenite using nanoindentation, Scr. Mater. 63 (2010) 540–543.
[40] Z. Lin, L. Wang, X. Xue, W. Lu, J. Qin, D. Zhang, Microstructure evolution and mechanical properties of a Ti–35Nb–3Zr–2Ta biomedical alloy processed by equal channel angular pressing (ECAP), Mater. Sci. Eng. C 33 (2013) 4551–4561.
[41] M. Okayasu, Y. Ohkura, S. Takeuchi, S. Takasu, H. Ohfuji, T. Shiraishi, A study of the mechanical properties of an Al-Si-cu alloy (ADC12) produced by various casting processes, Mater. Sci. Eng. A 543 (2012) 185–192.
[42] R. Yazdi, H.M. Ghasemi, C. Wang, A. Neville, Bio-corrosion behaviour of oxygen diffusion layer on Ti-6Al-4V during tribocorrosion, Corros. Sci. 128 (2017) 23–32.
[43] F.X. Xie, X.B. He, S.L. Cao, X. Lu, X.H. Qu, Structural characterization and electrochemical behavior of a laser-sintered porous Ti–10Mo alloy, Corros. Sci. 67 (2013) 217–224.
[44] S. Ammar, K. Ramesh, B. Vengadaesvaran, S. Ramesh, A.K. Arof, A novel coating material that uses nano-sized SiO2 particles to intensify hydrophobicity and corrosion protection properties, Electrochim. Acta 220 (2016) 417–426.
[45] A. Rasooli, M.S. Safavi, M.K. Hokmabad, Cr2O3 nanoparticles: a promising candidate to improve the mechanical properties and corrosion resistance of Ni-Co alloy coatings, Ceram. Int. 44 (2018) 6466–6473.
[46] M. Poorraeisi, A. Afshar, The study of electrodeposition of hydroxyapatite-ZrO2-TiO2 nanocomposite coatings on 316 stainless steel, Surf. Coat. Technol. 339 (2018) 199–207.
[47] C. Fonseca, M.A. Barbosa, Corrosion behaviour of titanium in biofluids containing H2O2 studied by electrochemical impedance spectroscopy, Corros. Sci. 43 (2001) 547–559.

[48] B. Yoo, K.R. Shin, D.Y. Hwang, D.H. Lee, D.H. Shin, Effect of surface roughness on leakage current and corrosion resistance of oxide layer on AZ91 Mg alloy prepared by plasma electrolytic oxidation, Appl. Surf. Sci. 256 (2010) 6667–6672.
[49] J.B. Jorcin, M.E. Orazem, N. Pébère, B. Tribollet, CPE analysis by local electrochemical impedance spectroscopy, Electrochim. Acta 51 (2006) 1473–1479.
[50] W.R. Osório, J.E. Spinelli, I.L. Ferreira, A. Garcia, The roles of macrosegregation and of dendritic array spacings on the electrochemical behavior of an Al-4.5 wt.% Cu alloy, Electrochim. Acta 52 (2007) 3265–3273.
[51] I. Milošev, G. Žerjav, J.M.C. Moreno, Electrochemical properties, chemical composition and thickness of passive film formed on novel Ti–20Nb–10Zr–5Ta alloy, Electrochim. Acta 99 (2013) 176–189.
[52] I.C. Lavos-Valereto, I. Costa, S. Wolynec, The electrochemical behavior of Ti-6Al-7Nb alloy with and without plasma-sprayed hydroxyapatite coating in Hank's solution, J. Biomed. Mater. Res. 63 (2002) 664–670.
[53] H.M.A. El-Lateef, M.K. Mai, Corrosion resistance of ZrO2 -TiO2 nanocomposite multilayer thin films coated on carbon steel in hydrochloric acid solution, Mater. Charact. 108 (2015) 29–41.
[54] M. Metikos-Huković, A. Kwokal, J. Piljac, The influence of niobium and vanadium on passivity of titanium-based implants in physiological solution, Biomaterials. 24 (2003) 3765–3775.
[55] J. Li, S.J. Li, Y.L. Hao, H.H. Huang, Y. Bai, Y.Q. Hao, Electrochemical and surface analyses of nanostructured Ti-24Nb-4Zr-8Snalloys in simulated body solution, Acta Biomater. 10 (2014) 2866–2875.
[56] R.S. Mishra, Z. Ma, I. Charit, Friction stir processing: a novel technique for fabrication of surface composite, Mater. Sci. Eng. A 341 (2003) 307–310.
[57] S.J. Li, R. Yang, S. Li, Y.L. Hao, Y.Y. Cui, M. Niinomi, Z.X. Guo, Wear characteristics of Ti-Nb-Ta-Zr and Ti-6Al-4V alloys for biomedical applications, Wear. 257 (2004) 869–876.
[58] M. Niinomi, Mechanical properties of biomedical titanium alloys, Mater. Sci. Eng. A 243 (1998) 231–236.
[59] A. Balyanov, J. Kutnyakova, N.A. Amirkhanova, V.V. Stolyarov, R.Z. Valiev, X.Z. Liao, Y.H. Zhao, Y.B. Jiang, H.F. Xu, T.C. Lowe, Y.T. Zhu, Corrosion resistance of ultrafine-grained Ti, Scr. Mater. 51 (2004) 225–229.
[60] R. Huang, H. Zhuang, Y. Han, Second-phase-dependent grain refinement in Ti-25Nb-3Mo-3Zr-2Sn alloy and its enhanced osteoblast response, Mater. Sci. Eng. C. 35 (2014) 144–152.
[61] A. Fattah-alhosseini, H. Elmkhah, G. Ansari, F. Attarzadeh, O. Imantalab, A comparison of electrochemical behavior of coated nanostructured Ta on Ti substrate with pure uncoated Ta in Ringer's physiological solution, J. Alloys Compd. 739 (2018) 918–925, https://doi.org/10.1016/j.jallcom.2017.12.339.
[62] M. Tahara, T. Inamura, H.Y. Kim, S. Miyazaki, H. Hosoda, Role of oxygen atoms in α″ martensite of Ti-20 at.% Nb alloy, Scr. Mater. 112 (2016) 15–18.
[63] R. Rajeshkumar, V. Udhayabanu, A. Srinivasan, K.R. Ravi, Microstructural evolution in ultrafine grained Al-graphite composite synthesized via combined use of ultrasonic treatment and friction stir processing, J. Alloys Compd. 726 (2017) 358–366.
[64] J. Lu, Y. Zhang, W. Huo, W. Zhang, Y. Zhao, Y. Zhang, Electrochemical corrosion characteristics and biocompatibility of nanostructured titanium for implants, Appl. Surf. Sci. 434 (2018) 63–72.